Significant Diurnal Warming Events Observed by Saildrone at High Latitudes

Chong Jia[1], Peter J. Minnett[2], and Bingkun Luo[2,3]

[1]Graduate Program of Meteorology and Physical Oceanography, Rosenstiel School of Marine, Atmospheric, and Earth Science, University of Miami, Miami, FL, USA.

[2]Department of Ocean Sciences, Rosenstiel School of Marine, Atmospheric, and Earth Science, University of Miami, Miami, FL, USA.

[3] Current address: Atomic and Molecular Physics Division, Harvard-Smithsonian Center for Astrophysics, Cambridge, MA, USA.

Corresponding author: Chong Jia (chong.jia@earth.miami.edu)

Key Points:

- Using skin and subsurface ocean temperatures from two Saildrones to study the 2 m upper ocean thermal stratifications at high latitudes.
- Several diurnal warming events with significantly large amplitudes, some even with long persistence, are documented and discussed.
- Model schemes for diurnal warming applied at high latitudes necessarily need to be improved.

Abstract

The sea surface temperature (SST) is one of the essential parameters to understand the climate change in the Arctic. Saildrone, an advanced autonomous surface vehicle (ASV), has proven to be a useful tool for providing sufficiently accurate SST data at high latitudes. Here, data from two Saildrones, deployed in the Arctic in the summer of 2019, are used to investigate the diurnal variability of upper ocean thermal structure. An empirical cool skin effect model with dependence on the wind speed with new coefficients was generated. Several local large diurnal warming events were observed, the amplitudes of warming in the skin layer > 5 K, rarely reported in previous studies. Furthermore, the warming signals could persist beyond one day. For those cases, it was found surface warm air suppressed the surface turbulent heat loss to maintain the persistence of diurnal warming under low wind conditions. Salinity also plays an important role in the formation of upper ocean density stratification during diurnal warming at high latitudes. A less salty surface layer was likely created by precipitation or melting sea ice, providing favorable conditions for the formation of upper ocean stratification. By comparing with two prognostic diurnal warming models, the simulations match reasonably well with those from the Saildrone for moderate wind speed conditions but exhibit large differences at low winds. Both schemes show significant negative biases in the early morning and late afternoon. It is necessary to further improve the model schemes when applied at high latitudes.

Plain Language Summary

At high latitudes, satellite remote sensing retrieval of SST is challenging and the number of drifting buoys measuring in situ temperatures is also sparser than elsewhere. Two Saildrone cruises in 2019 summer, carrying a suite of scientific instruments onboard, can offer both accurate skin SST and subsurface SST measurements at the Pacific sector of Arctic. This study concentrates on those data along with associated atmospheric parameters to demonstrate the characteristics of diurnal variability of temperatures in the upper 2 m ocean. That the Arctic is warming much faster than elsewhere as a result of temperature-dependent feedbacks, emphasizing the need for a better understanding of the thermal structure of the upper Arctic Ocean. Furthermore, comparisons with model simulations reveal that the diurnal warming schemes for high latitudes still need to be improved.

1 Introduction

Sea surface temperature (SST) is affected by many factors including ocean thermodynamic and hydrodynamic processes and air-sea interactions, and is one of the most important parameters governing the exchange of gases, heat, and momentum at the air-sea interface. As shown in Figure 1, SST is not a unique definition of the surface ocean temperature due to the complicated and variable vertical thermal structure in the uppermost ocean (~10 m). There is nearly always a thermally stratified thin layer, commonly known as the cool skin layer, caused by upward heat flux from the ocean to atmosphere and molecular conduction dominates the heat flow within the layer (*Donlon et al.*, 2007). Such a "skin" layer results in a cooler skin SST (SST_{skin}) compared to the sub-skin SST ($SST_{subskin}$), giving a difference typically ranging from 0.1 to 0.3 K (*Gentemann and*

Minnett, 2008). In the mixed layer, which is below the skin layer, turbulence is no longer restrained by the large air-sea density difference and near surface viscosity that leads to the viscous sublayer just below the interface, and tends to cause turbulent mixing resulting in very small vertical temperature gradients (Figure 1; profile in red). Nevertheless, thermal stratification can be sustained by insolation since most of the incoming solar radiation is absorbed by the top several meters of the upper ocean during the day (Figure 1; profile in black). This diurnal thermocline, the stratified layer due to diurnal warming, has been studied for several decades (*Donlon et al.*, 2002; *Merchant et al.*, 2008; *Schluessel et al.*, 1990; *Sverdrup et al.*, 1942). The surface SST_{skin} has been found to be more than 3 K, even up to 6 K, warmer when referenced to the foundation temperature (SST_{fnd}), which is the temperature free of diurnal variability (*Gentemann et al.*, 2008; *Kawai and Wada*, 2007; *Minnett*, 2003). Such large amplitudes of diurnal heating signals are not rare and may last for several hours.

Early studies of the ocean surface diurnal warming were primarily in lower latitudes (*Halpern and Reed*, 1976; *Stommel and Woodcock*, 1951) as large-scale atmospheric circulation in the tropics is strongly affected by small variability in SSTs (*Shukla*, 1998). In recent years, researchers have paid more attention to the mid-latitudes, such as the Mediterranean Sea (*Böhm et al.*, 1991; *Deschamps and Frouin*, 1984; *Merchant et al.*, 2008), the eastern North Pacific off California (*Flament et al.*, 1994; *Price et al.*, 1986), and elsewhere in the global ocean (*Gentemann et al.*, 2008; *Stramma et al.*, 1986). However, very few papers have demonstrated diurnal warming at high latitudes. Some of the studies of high latitude areas indicate a few diurnal warming signals in either satellite-derived SST (*Kawai and Wada*, 2007) or drifting buoy data (*Kennedy et al.*, 2007). *Eastwood et al.* (2011) investigated the diurnal warming events in the Arctic, mostly in the Atlantic sector (30ºW-30ºE), during summer months in 2008. At somewhat lower latitudes, *Karagali et al.* (2012) identified and characterized the diurnal warming at the sea surface in the North Sea and the Baltic Sea.

To examine the diurnal warming in the upper ocean, measurements of SSTs with sufficient accuracy are essential. The SSTs could be generally categorized into two groups, i.e., SST within the skin layer (SST_{skin}) and SST beneath the skin layer ($SST_{subskin}$ or SST_{depth}). SST_{skin} is usually taken as the temperature measured by satellite-based or ship-borne infrared (IR) radiometers that detect emission from a layer ~10-100 μm beneath the air-sea interface, while $SST_{subskin}$ denotes the temperature at the base of the conduction-dominated skin layer and can be approximated as the retrieval of SST by microwave radiometers. SST_{depth} represents the ocean temperature beneath $SST_{subskin}$ at depths of a few centimeters to a few meters utilizing contact thermometers on various platforms such as Argo floats, drifting buoys, moorings and ships (*Xu and Ignatov*, 2014). For the polar regions, the main challenges of IR satellite SST_{skin} retrievals are the frequent and persistent clouds (*Key et al.*, 2004; *Shupe et al.*, 2011), compensations for the extreme air conditions in the atmospheric correction algorithm (*Jia and Minnett*, 2020; *Vincent et al.*, 2008b; *Vincent et al.*, 2008a), and sea ice contamination (*Høyer et al.*, 2012). The limitation of the field measurements of SST_{depth} is basically due to sparse coverage, especially at the Pacific sector (150ºE-150ºW) of the Arctic.

Another relatively new technology, autonomous underwater vehicles (AUVs), has been applied to collect the oceanographic data and analyze the diurnal warm layer (*Hodges and Fratantoni*, 2014; *Matthews et al.*, 2014; *Ward et al.*, 2014). Recently, a more advanced and capable observing platform, Saildrone, an autonomous surface vehicle (ASV), provides vertical samples with high-resolution temporal evolutions of the upper-ocean warming events (*Gentemann et al.*, 2020). Meanwhile, Saildrone ASVs are also able to simultaneously measure the ancillary meteorological variables, including wind speed which is directly related to the vertical distribution of heat. To better understand the temperature variability at the skin layer and at depth at high latitudes, the data from Saildrones during two Arctic cruises in 2019 can be used. This work presents information on the formation of warming events at the Pacific sector in the Arctic, which have been barely sampled in previous studies. To our knowledge, it is also the first investigation of the upper-ocean thermal variability with the Saildrone ASV measurements at high latitudes. Diurnal signals were identified in Saildrone data taken off Southern California and Baja California in 2018 (*Gentemann et al.*, 2020).

This paper is structured as follows. An introduction to the Saildrone Arctic cruises in 2019 along with the data descriptions are presented in Section 2. Some significant and representative warming events are identified and analyzed in Section 3. A discussion of the measurements is given in Section 4. Conclusions are summarized in Section 5.

2 Data

The research presented here is mainly based on SSTs (both SST_{skin} and SST_{depth}) of the upper 2 m in the ocean and relevant near-surface meteorological parameters measured by Saildrone ASVs from 15 May to 11 October 2019 as part of the Multi-sensor Improved Sea-Surface Temperature (MISST) project (*Gentemann et al.*, 2018). In a joint NOAA-NASA deployment, the 2019 Arctic cruises consisted of six Saildrones, departing from Dutch Harbor, Alaska, five of which passed through the Bering Strait into the Chukchi Sea, several times approaching the ice edge of the Arctic Ocean (up to ~75ºN) before turning back. The Saildrone is a wind-driven ASV manufactured by Saildrone, Inc. (Alameda, CA), collecting high-resolution data with a suite of onboard solar-powered oceanographic and meteorological sensors. Each vehicle, a Saildrone Explorer, weighs ~750 kg, consisting of a 7 m long hull, a 5 m tall wing and a keel with a 2.5 m draft, travelling at an average speed of 2 m/s. More detailed descriptions of the Saildrone can be found in *Meinig et al.* (2019). Here, measurements from two of the Saildrones, SD-1036 and SD-1037, funded by NASA through the National Oceanographic Partnership Program (NOPP) are used for studying the diurnal warming at high latitudes. The navigation routes are shown in Figure 2, and the configuration of these two Saildrones is illustrated in Figure 3.

2.1 SST Dataset

2.1.1 Skin Temperatures (SST_{skin})

Unlike all but one of the previously deployed Saildrones (*Mordy et al.*, 2017; *Vazquez-Cuervo et al.*, 2019), and also different from the other four vehicles in this Arctic expedition, SD-1036 and

SD-1037 were equipped with dual IR radiometers, intended to facilitate the derivation of SST_{skin} measurements. Two Heitronics IR pyrometers operating in the range of wavelengths from 8 to 14 μm were installed on the foredeck at a height of 0.8 m above the waterline as a pair, one viewing the sea surface, a model CT15.10 (CT15 hereafter) and the other directed towards the sky, a model CT09.10 (CT09 hereafter). In common with most other Saildrones, an additional CT15 was mounted on the wing spar at the height of 2.25 m above the waterline. Since the IR spectral radiance measured by sea-viewing CT15 pyrometers include a component of atmospheric downwelling radiance reflected at the ocean surface, the measurements of CT09, pointing at the same zenith angle as the sea-viewing senor to the nadir, can be used to correct for the sky radiance reflection in CT15. The sea-viewing measurement is expressed as:

$$R_{sea} = \int_{\lambda_1}^{\lambda_2} \eta(\lambda) \left[\varepsilon(\lambda,\theta)B(T_{skin},\lambda) + (1-\varepsilon(\lambda,\theta))B(T_{sky},\lambda)\right]d\lambda \quad (1)$$

$$R_{sea} = \int_{\lambda_1}^{\lambda_2} \eta(\lambda)B(T_{sea},\lambda)\,d\lambda \quad (2)$$

where T_{sea} and T_{sky} are the IR radiometric temperatures output from CT15 and CT09, and $B(T,\lambda)$ represents the Planck function. $\varepsilon(\lambda,\theta)$ is the sea surface emissivity, primarily a function of the wavelength λ and zenith angle θ. $\eta(\lambda)$ is the normalized spectral response function of each CT15 sensor, which defines the limits of integration in (1) and (2). T_{skin} is thus the derived SST_{skin}.
Based on the equations above, *Jia et al.* (2022) rigorously determined the SST_{skin} using the data from SD-1036 and SD-1037, considering the effects of varying viewing geometry due to Saildrone tilts. After analyzing the error budget, the SST_{skin} derivations are proven to be sufficiently accurate (~0.1 K) for scientific research after excluding measurements contaminated by nearby sea ice or during or shortly after precipitation. Therefore, these data can be utilized to examine the evolution of the warming signals in the skin layer, and to calculate air-sea heat fluxes.

2.1.2 Subsurface Temperatures (SST_{depth})

For the subsurface SST measurements, each Saildrone carried two CTDs (Conductivity, Temperature, and Depth) instruments during the Arctic cruise in 2019. The SBE 37-SMP-ODO MicroCAT is a high-accuracy CTD recorder manufactured by Sea-Bird Scientific for long-duration deployments. The RBRconcerto^3 is also a reliable, self-contained CTD manufactured by RBR taking measurements at 1-minute sampling intervals. Note that the RBR CTD was attached with an additional RBRcoda^3 temperature and optical dissolved oxygen (T.ODO) sensor, but here we consider only the temperature measurements. The stated accuracy of temperature data from all the three sources is ± 0.002 K. Both SBE 37 and RBR CTDs were installed on the two sides of the keel, at -0.54 m below the sea surface when the Saildrone is upright. For this reason, intercomparisons were made for data measured away from sea ice, which can be identified by the onboard cameras. The statistics are listed in Table 1. The three sensors have very small biases relative to each other, especially between the two CTDs, indicating their good measurement capability. However, the standard deviations are higher than expected resulting from some distinct fluctuations at certain days shown in Figure 4 (in red). Those are attributed to increased and more

variable near surface temperature stratification, also demonstrated in Figure 4 (in blue) as the difference between skin and sub-surface temperatures. Because of the vehicles' rolling, the sensors would deviate from the nominal installation depth and measure at different depths. Even for a small inclination, SSTs simultaneously taken by the SBE 37 and RBR CTDs could have significant discrepancies as a result of the presence of intensified upper-ocean stratification.

Seven Sea-Bird SBE 56 internally-recording temperature loggers were set at different depths along the keel for each Saildrone, at -0.33 m, -0.47 m, -0.81 m, -1.04 m, -1.20 m, -1.42 m and -1.71 m. Those data combined with the IR radiometer-derived SST_{skin} and CTD measurements, can provide good samplings of the vertical profiles of the upper-ocean temperature. The SBE 56 sensor at -1.04 m on SD-1036 and the one at -0.47 m on SD-1037 did not function. The lowest three SBE 56 sensors on SD-1037 have been corrected for a time stamp error in the recordings, apparently caused by the internal clock being set to local time and not to UTC. As shown in Figure 4, although there were no SST_{skin} retrievals for SD-1036 after early August as a result of solar power constraints, the prominent thermal stratification events were concentrated in June and July. Considering data from periods with no clear thermal stratification, the accuracy of SSTs at various depths can be determined by comparison with the temperatures from the deepest SBE 56 (Table 2). The mean biases (standard deviations) for the other SBE 56s are no more than 0.02 K (0.16 K). The SBE 37 and RBR CTDs also show good agreement, while the RBR T.ODO has a larger bias of 0.028 K. The SST_{skin} data from days free of thermal stratification are expected to be cooler than SST_{depth} by ~0.17 K because of the skin effect (*Donlon et al.*, 2002). The results in Table 2 are very close to that expected value, indicating an appropriate correction for the reflected sky radiation by *Jia et al.* (2022).

2.2 Meteorological Variables

Several papers have reported the accuracy of the meteorological parameters collected aboard the Saildrones deployed on previous cruises (*Gentemann et al.*, 2020; *Meinig et al.*, 2015; *Zhang, D et al.*, 2019). The measurements show reasonable agreement with the data from nearby ship or buoy platforms, and the differences are mainly related to separation distance and a passing sub-synoptic scale weather system (*Zhang, D et al.*, 2019).

Both SD-1036 and SD-1037 employed an ultrasonic Gill Anemometer 1590-PK-020, located at the top of the wing at 5 m above the sea surface, measuring the three-dimensional wind vector. The corrections for the vehicle motion were done in real time, using the onboard GPS inertial navigation system (INS) and inertial measurement units (IMUs) to provide samples relative to fixed Earth coordinates. The instantaneous wind measurement heights were also determined considering the tilt of wing given by the IMU data.

The barometric pressure was measured by a Vaisala Barometer PTB210 mounted on the hull at a height of 0.2 m. In view of the earlier experience (a constant bias of -13hPa) shown in *Gentemann et al.* (2020), the air pressure sensor was sheathed in a water-repellent box with a vent, protecting the instrument from moisture infiltration.

For air temperature (T_{air}) and relative humidity (RH), Saildrones are equipped with a Rotronic HC2-S3 probe on the spar at a height of 2.3 m. The humidity and temperature instrument is

sensitive to air flow since the self-heating effect in low wind conditions would cause larger errors (*Zhang, D et al.*, 2019).

An LI-192 Quantum Sensor was installed on the spar at 2.6 m height, measuring the Photosynthetically Active Radiation (PAR), which is the amount of solar radiation available for driving photosynthesis in the wavelength range from 400 to 700 nm, and is often considered to be 40-60% of the total incoming shortwave radiation depending on cloud cover and solar angle. Without the use of gimbals, the LI-192 PAR measurements could have significant offsets due to the tilt of the Saildrone from horizontal, resulting in the changed angular orientation of direct beam irradiance to the sensor (*Nunez et al.*, 2022). However, the platform inclinations were small during most of the time in the periods studied here. Therefore, we argue that the PAR data do not necessarily need to be corrected for the tilting effect, and errors can be reduced by replacing values taken with large rolling angles with interpolated ones. The following formula is used to convert PAR into shortwave solar radiation, considering the robust relationship between the two parameters (D. Zhang, Pers. Comm., 2022):

$$\mathrm{Solar} = \mathrm{PAR}/2.4 \tag{3}$$

where the PAR is measured in μmol/(m^2·s), and the solar radiation is in units of W/m^2.

3 Thermal Effects in the Upper Layer

According to the profiles shown in Figure 1, the approximated temperature at the ocean-atmosphere interface, SST_{skin}, can be defined as the combination of subsurface temperature, SST_{depth}, cool skin effect, ΔT_c, and warming if present in the depth z of the ocean, ΔT_w:

$$SST_{skin} = SST_{depth}(z) + \Delta T_c + \Delta T_w(z) \tag{4}$$

where SST_{skin} is derived from the IR pyrometers, SST_{depth} is measured at depth by a CTD or a temperature logger installed on the keels of the Saildrones.

3.1 Cool Skin

The cool skin effect, resulting from the oceanic heat loss given by the exchange of net longwave radiation, sensible and latent heat fluxes (*Saunders*, 1967), is nearly present throughout the day and night. ΔT_c can be parameterized with a simple model in dependence on the wind speed. *Donlon et al.* (2002) (hereafter D2002) used an exponential equation characterizing SST_{skin} minus SST_{depth} as a function of 10 m wind speed (U_{10}). Subsequent studies (*Alappattu et al.*, 2017; *Luo et al.*, 2022; *Minnett et al.*, 2011 (M2011); *Zhang, H et al.*, 2020 (Z2020)) fitted their data in the same formulation but with different coefficients. Figure 5 demonstrates the wind dependence of cool skin temperature difference referenced to the $SST_{-1.71\ m}$ along with the least squares fitting and the parameterizations from D2002, M2011, and Z2020. Those nighttime data are from both SD-1036 and SD-1037 and are selected for solar elevation angles below -10º. The logarithmic wind profile converts the anemometer measurements to U_{10}. The fitted curve shows remarkable agreement with the results of D2002, M2011 and Z2020 except for low wind speeds (< 3 m/s), indicating that cooling in the skin layer with little influence of mechanical mixing induced by wind stress is acting differently under different conditions in the global ocean. Z2020 shows a slightly larger cool skin amplitude in general (0.02 K), but definitely within the measurement uncertainty. Therefore, the

new parameterizations are physically reasonable and would be used to estimate the cool skin effect for all the data in this study:

$$\Delta T_c = -0.15 - 0.41 * \exp(-U_{10}/2.5) \quad (5)$$

3.2 Diurnal Warming

Upper ocean heating and cooling on a diurnal cycle is a frequently observed feature of the oceans at low- and mid-latitudes. Although usually referred to as diurnal heating or warming, an important part of the process is the cooling that results from the reduction of insolation as the solar zenith angle increases in the afternoon and evening, and from the absence of solar heating during the night. The result of the cooling part of the cycle is to distribute the daily gain or loss of heat through a deeper layer and thus make the SST signal relative to the start of the heating very small. It might be questioned whether "diurnal heating" is an appropriate term to be used for high-latitude summer conditions when the sun is always above the horizon for weeks to months. Because of the smaller heat loss during the cooling part of each cycle, there may be situations where the diurnal heating signal may extend over more than a single day.

Based on (4) and (5), the magnitudes of diurnal warming in the top 1.7 m of the upper ocean layer can be estimated. Some significant diurnal warming events were observed by two Saildrones SD-1036 and SD-1037 as shown in Figure 6. Those were identified when the warming amplitudes > 2 K lasted for at least one hour. SD-1036 had 13 days with significant diurnal warming signals, and SD-1037 had 12 days. Given the small separations between the two vehicles during these periods, significant warming was often found on the same days in the measurements from both Saildrones. Figure 6 illustrates the solar insolation and warming amplitudes colored by simultaneously measured wind speeds as a function of local mean time (LMT). The large warming events were as a result of strong solar radiation and little near-surface mixing due to low wind speeds. For wind speed > 8 m/s, the surface warming signature almost vanished as the heat was mixed throughout a layer deeper than our deepest sensor. Since the temperature in the warmed layer is a result of accumulated heat, it is not necessary that the maximum temperature occurs at the same time as the maximum insolation, and the temperature can continue to rise even after the insolation has peaked. Moreover, the temperature is strongly dependent on wind, so an increase in the wind speed prior to the maximum insolation can result in the accumulated heat being mixed deeper, leading to a situation when the maximum temperature occurs before the maximum insolation. Thus, in our data the highest temperatures of a day usually did not occur at the time of the strongest insolation, but with a lead or delay of time depending on wind speed. Furthermore, some diurnal warming persisted from one day into the next on 15-16 June and 8-9 July due to the midnight sun in the Arctic accompanied by low winds. Some cases are examined below to show the characteristics of upper ocean thermal stratifications and air-sea interaction.

Figure 7a shows the diurnal warming that occurred on 19 May 2019 observed by SD-1036, which was the first prominent diurnal warming event captured by both Saildrones during the mission. The largest measured warming amplitude was about 5 K, under a wind speed of 0.6 m/s and solar radiation of 751 W/m^2 at 10:58 LMT. The incoming insolation reached a maximum value of 843 W/m^2 at 10:53 LMT and was rapidly diminished by clouds after the peak, resulting in the

accompanying decrease of surface warming with low but slightly increasing wind speeds. At 14:10 LMT, the insolation began to increase again due to thinning clouds, causing a secondary peak in the diurnal warming. Note that the wind speed was also about to increase at that time, thus the magnitude of second peak was just 1.6 K. Finally, the wind induced mixing totally erased the warming in the skin layer of the ocean at 19:50 LMT as the wind speed reached up to 7 m/s. Figure 7b provides the diurnal variabilities of both vertical temperature profile in the top 1.7 m of ocean and surface air temperature. Before 6:00 LMT, the cool skin effect was dominant, with isothermal water below, but subsequently as the oceanic heat gain exceeded heat loss due to the increase of incoming solar radiation, the SST_{skin} became warmer than subsurface SSTs taken by the keel-mounted SBE 56 temperature loggers at different depths. The warming was mostly concentrated at the surface at first, and deepened as the heat was further transferred down, leading to a distinct delay of warming response in the mixed layer, with the peak of $SST_{-0.33\ m}$ 31 min later than that of SST_{skin}. Generally, the surface air temperatures varied consistently along with the diurnal cycle of SST_{skin}, but were always cooler throughout the day. The source of the air was simulated by the widely-used Hybrid Single-Particle Lagrangian Integrated Trajectory (HYSPLIT) model, developed by NOAA's Air Resources Laboratory for atmospheric trajectory and dispersion calculations (*Stein et al.*, 2015). The backward trajectories in Figure 7e indicate the cold air came from Northeast Siberia in the Arctic, and Figure 7f further demonstrates that the Siberian air at higher altitudes was transferred southward to the Bering Sea by descending advection. Using the Coupled Ocean–Atmosphere Response Experiment (COARE) bulk algorithm version 3.6 (*Edson et al.*, 2013; *Fairall et al.*, 2003), surface sensible and latent heat fluxes were calculated (Figure 7c). The heat fluxes are defined as positive upward, from the ocean surface to the atmosphere. A greater proportion of the available energy at ocean surface was passed to the atmosphere as latent heat due to seawater evaporation than as sensible heat induced by the air-sea temperature difference. The surface turbulent heat loss from the ocean persisted due to the presence of cold and dry air from Siberia, and reached a maximum at 11:07 LMT, slightly later than the peak of diurnal warming. At low temperatures, the seawater density depends much more on salinity rather than temperature. Therefore, the salinity could play an important role in the formation of upper ocean stratifications during the diurnal warming at high latitudes. The Saildrone onboard cameras recorded a precipitation event in the local area on 18 May, as shown in Figure 7d. The rain will have lowered the salinity of a thin layer at the surface ocean, where the absorption of shortwave radiation increased and the heat was trapped, causing strong warming signals within the skin layer but a delay and much weaker response in the water beneath.

Figure 8a shows another significant diurnal warming on 15-16 June observed by SD-1036, with a peak of 5.1 K at a wind speed of 0.9 m/s on 15 June at 14:01 LMT, then maintaining the strong warming signal into the next day. The wind speed decreased as the insolation increased on the first day until evening. After that, the wind began to increase and eroded the surface warming. The diurnal warming had not vanished the next morning and remained through much of the day as the sunlight intensified, even though the wind had reached 4 m/s. There was a second peak in warming near the noon due to a drop in the wind speed. The warming was completely erased by the upper layer mixing and surface turbulent heat loss as the wind continued to increase up to 8 m/s. Figure

8b illustrates the warming spread much deeper than the case in Figure 7b, with the evident divergence of ocean temperatures at different depths. SST_{skin} was already warmer than SST_{depth} early in the morning, which could be explained by the midnight sun in the summertime Arctic. The 2 m air temperature was higher than SST_{depth} before noon on 16 June, even higher than SST_{skin} at some times. Based on HYSPLIT back-trajectories, such warm air originated from the lower atmosphere over the Arctic Ocean but was heated by its passage over land, as shown in Figures 8e and 8f. The backward trajectory starting at 6:00 LMT on 16 June missed passing over land, indicating the local surface air temperature dropped due to the sinking cold air from higher latitudes (Figure 8f), which could also be verified in Figure 8b. The calculated surface heat fluxes in Figure 8c further demonstrate the warm air effects, that the sensible heat was small or even negative indicating heat gain from the atmosphere, and the magnitude of latent heat was low as well before the air became cool and dry. Such low surface turbulent heat loss contributed to sustaining the diurnal warming into the next day. Figure 8d indicates the warming event from 15 to 16 June occurred close to the marginal ice zone (MIZ), where a less salty surface layer was likely created by melting sea ice, providing favorable conditions for the formation of upper ocean stratification.

The diurnal warming held for more than one day again on 8-9 July 2019. Figure 9a shows the measurements from SD-1037, with a peak of 7.4 K, the maximum signal captured during the entire cruises, at a wind speed of 1.6 m/s on 8 July at 17:31 LMT. Different from Figures 7a and 8a, the variation of surface warming is not so smooth with some large fluctuations due to the spatial variability of SSTs in the top 1.7 m of the ocean (Figure 9b), indicating the complexity of local water mass structure. The warm surface air temperature restrained the surface turbulent heat loss to maintain the persistence of diurnal warming under low wind conditions as shown in Figure 9c. The warm air was traced back to the descending cold air flowing northward and heated over Siberia (Figures 9e and 9f). The backward trajectory beginning at 6:00 LMT on 9 July reached a higher latitude first before reaching the Saildrone, indicating the local surface air began to be cooled, consistent with the measurements in Figure 9b. As illustrated in Figure 9d, there was no rainfall at an earlier time, nor sea ice in the vicinity, only a clear and sunny sky, indicating that stabilizing the near-surface water by lower salinities from precipitation or local ice melt is not a necessary condition for large amplitude diurnal heating.

3.3 Model Comparison

The events described above show large diurnal heating magnitudes can be as large as 5 K, which were previously rarely observed in the Arctic region by either satellites or in situ instruments. Simulations produced by diurnal warming models, useful tools to estimate the daily change in SST_{skin}, coupled with cool skin effect, are compared with the diurnal warming calculated from Saildrone SST_{skin} measurements, using the oceanic and atmospheric variables measured by the Saildrones as the required model inputs. Two prognostic models presented by *Zeng and Beljaars* (2005) (hereafter ZB05) and *Akella et al.* (2017) (hereafter AK17) are used in this study. The ZB05 scheme has been implemented in the European Center for Medium-Range Weather Forecasts (ECMWF) atmospheric general circulation model (AGCM) and was shown to have a beneficial

impact on the mean climatologies (*Brunke et al.*, 2008) in the Community Atmosphere Model version 3.1 (CAM3.1). The AK17 model is a development of the *Takaya et al.* (2010) model, itself an improved version of ZB05 with changes to the similarity function for stable conditions and an additional Langmuir circulation effect (*McWilliams and Sullivan*, 2000). To minimize the effect of noise in the measurements, the inputs into the models were preprocessed with a low-pass filter by taking 10-min averages. Figure 10a shows the diurnal warming events observed in the SST_{skin} by SD-1036 as well as the corresponding model simulations by ZB05 and AK17. Generally, the maximum warming amplitudes simulated by AK17 are more comparable to the Saildrone measurements, while ZB05 gives a clear overestimation above 1.5 K on average. The deficiencies in warming amplitude estimation by ZB05 have been identified and reported by *Bellenger and Duvel* (2009), which might be attributed to the fixed and sharp temperature profile used in the model (*Bellenger and Duvel*, 2009), and modified by *Takaya et al.* (2010) with the refinements mentioned earlier. The AK17 simulation is very sensitive to the wind speed, and the heating signal decays too quickly with the increase of wind speed (*Gentemann and Akella*, 2018). Furthermore, the simulated diurnal warming drops overly rapidly in the late afternoon resulting in underestimation of the signal although AK17 does not follow the ZB05 scheme to obtain a slow decay of diurnal warming in the late afternoon (*Akella et al.*, 2017). Both models failed to simulate the warming signals holding beyond one day, indicating the lack of appropriate a priori knowledge of diurnal SST evolution at high latitudes during polar day with 24 hours of sunlight in the prognostic models. Excluding those consecutive days with persistent existence of warming, Figures 10b and 10c show the ZB05/AK17 model - Saildrone diurnal warming difference as a function of U_{10} and the LMT in hour of the day. As shown in Figure 10b, the model results match reasonably well with those from the Saildrone for moderate wind speed conditions ($U_{10} > 4$ m/s), however, the extremely large differences are concentrated at low winds ($U_{10} < 3$ m/s), indicating the inappropriate vertical temperature profile assumption for the weak mixing in the subsurface layer. Similar results were also found by *Luo et al.* (2022). ZB05 has large positive biases around the midday and AK17 shows significant negative biases in the late afternoon (Figure 10c) due to the unrealistically rapid decay of warming. Both schemes present the ocean surface is cooling in the early morning and late evening, which might not be the case in the summer Arctic as a result of the midnight sun.

Overall, AK17 simulated diurnal warming deviated from the Saildrone observations with a root mean square error (RMSE) of 0.6 K, smaller than ZB05 which had an RMSE of 1.1 K, indicating that it is necessary to further improve both model schemes for diurnal warming, especially when applied at high latitudes. Nevertheless, the model-Saildrone diurnal warming difference cannot be totally attributed to imperfections of the models. A potential problem is the navigation of the Saildrone vehicle, that is to say some spatial variability in measured variables along the track could be aliased as temporal changes. Inaccuracies in the input solar radiation and turbulent heat fluxes could influence the magnitude of simulations (*Takaya et al.*, 2010). In addition, the cool skin effect estimated from (5) also introduces some uncertainties in the diurnal warming observed by the Saildrones.

4 Summary and Discussion

Climate change is amplified at high latitudes relative to lower latitudes. According to numerical climate model simulations, the largest contribution to Arctic Amplification was found to be from enhanced temperature feedbacks rather than the surface albedo feedback mechanism (*Pithan and Mauritsen*, 2014), indicating that SST is one of the key parameters to understand the climate change in the Arctic. Saildrone, an advanced ASV, has proven to be capable of measuring sufficiently accurate SST data at high latitudes (*Jia et al.*, 2022). This paper used both SST_{skin} and SST_{depth} as well as some auxiliary meteorological variables from two Saildrones, SD-1036 and SD-1037, deployed in the Arctic from Alaska in the summer of 2019 to study the diurnal variability of upper ocean thermal stratifications.

First of all, an empirical cool skin effect model with new coefficients was derived based on the same form of exponential function as D2002 and others. Compared with D2002 (M2011; Z2020), the new parameterization only shows a difference in the high wind speed asymptote of 0.01 K (0.02K; 0 K), but significant deviations at low wind speeds (< 3 m/s), indicating that the cool skin layer effect with little influence of wind-driven turbulent mixing is more variable. With the newly generated cool skin model, the amplitude of diurnal warming in the uppermost ocean of 1.7 m, the measuring depth of the deepest SBE 56 temperature logger, could be calculated using (4) and (5). Removing the periods when the Saildrones were approaching the sea ice and considering that some payloads had to be turned off or had reduced sampling intervals due to lack of sunlight after mid-August, SD-1036 and SD-1037 have 79 and 112 effective days in total with adequate diurnal warming calculations. Table 3 shows the distribution of the daily maximum diurnal warming for the effective days. The occurrence of diurnal warming events > 1 K were up to about 45% observed by both vehicles during the 2019 Arctic cruise, even including extremely large amplitudes > 5 K, rarely reported in the previous studies of high latitudes. Note that using the $SST_{-1.7\ m}$ as a baseline yields an accurate measurement of the diurnal stratification at shallower depths, but the warming could extend further than the deepest temperature, implying the estimation of diurnal warming to be conservative at times. Besides the significant magnitude of warming, some long-lasting signals were found, such as from 15 to 16 June and from 8 to 9 July. On the one hand, the relatively low wind speed and midnight sun supported the stratified upper ocean persisting into the next day. On the other hand, the local warm surface air, even warmer than SST_{skin}, could suppress the turbulent heat loss from the skin layer of ocean into atmosphere. As simulated by the HYSPLIT model in Figures 8 and 9, such surface air could originate from either lower or higher latitudes warmed by passage over land.

Since the seawater density depends much more on salinity than the temperature at lower temperatures, salinity plays a significant part in the formation of upper ocean stratifications during the diurnal warming at high latitudes. A stratified, less salty surface layer in the ocean was inferred to be present before several warming cases. According to the images recorded by the cameras onboard, the diurnal warming events on 19 May, 28 June and 18 July occurred straight after rainfall, while those on 16 June, 18 June and 17 July were adjacent to the MIZ. In contrast to the effect of melting sea ice, precipitation should decrease the salinity of a much thinner layer at the ocean surface, trapping heat into the layer and resulting in a shallow warming penetration depth, such as

shown in Figure 7b. The freshwater generated by sea ice melt could accumulate in the upper tens of meters of the ocean (*Peralta-Ferriz and Woodgate*, 2015), much thicker than the warm layer thickness of a few meters. Thus, we infer the thermal structure tends to be unstable due to the small difference in density between stratified layers caused by a small vertical gradient of salinity. Figure 8b demonstrates the stability of stratifications was weak during the existence of diurnal warming, and the high-frequency fluctuations of SST_{depth} indicate some vertical mixing in response to forcing by some factors, but not likely the wind in view of the low wind speed. Similar features are also identified in Figure 9b. The mechanism of this pattern is worth studying in the future with more information about the salinity profile, such as that could be obtained with multiple CTDs on the keels of Saildrones.

Running two prognostic diurnal warming models, ZB05 and AK17, shows that the simulated results match reasonably well with Saildrone observations under moderate wind speed conditions but with large differences at low winds. Both models fail to simulate the warming signals holding beyond one day. Both schemes show significant negative biases in the early morning and late afternoon, but ZB05 obviously overestimates the amplitude of warming especially around noon, even up to 2 K. Compared with Saildrone, AK17 gives simulations with an RMSE of 0.6 K, while ZB05 has an RMSE of 1.1 K. Therefore, it is essential to further improve both models when applied at high latitude regions, such as parameterizing the vertical ocean temperature profiles (*Gentemann et al.*, 2009) and considering the near-surface salinity profiles, adding a representative ocean wave model to consider the surface turbulent mixing due to wave breaking (*Takaya et al.*, 2010), and adjusting the coefficients controlling the heat mixing in the upper layer to obtain more realistic manner as shown in the in situ measurements (*Gentemann and Akella*, 2018).

Acknowledgments

We acknowledge the support of Saildrone Inc. This research was funded in part by a NASA contribution to the National Oceanographic Partnership Program (NOPP) Multi-sensor Improved Sea-Surface Temperature (MISST) project, Lead PI: Dr. Chelle Gentemann, The Farallon Institute, through contract 80NSSC20K0768. Chong Jia MS was a University of Miami Graduate School Fellow.

Data Availability Statement

The data for 2019 Saildrone Arctic Cruise are openly available from the NASA Physical Oceanography Distributed Active Archive Center at https://doi.org/10.5067/SDRON-NOPP0

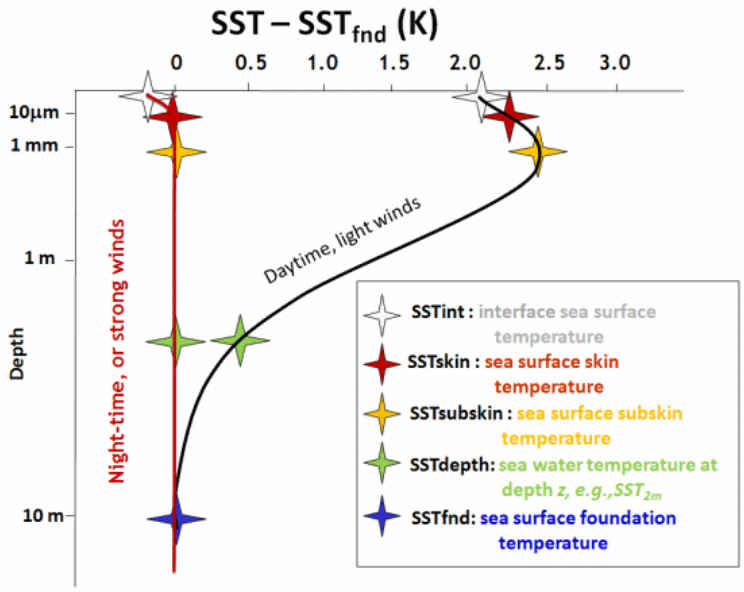

Fig. 1. The schematic diagram of the vertical temperature profile in the upper ocean during nighttime or daytime with strong wind-induced mixing (red line), and daytime with a well stratified diurnal warm layer (black line). Note that the scales for both axes are just for guidance and vary under different conditions. From *Minnett and Kaiser-Weiss* (2012).

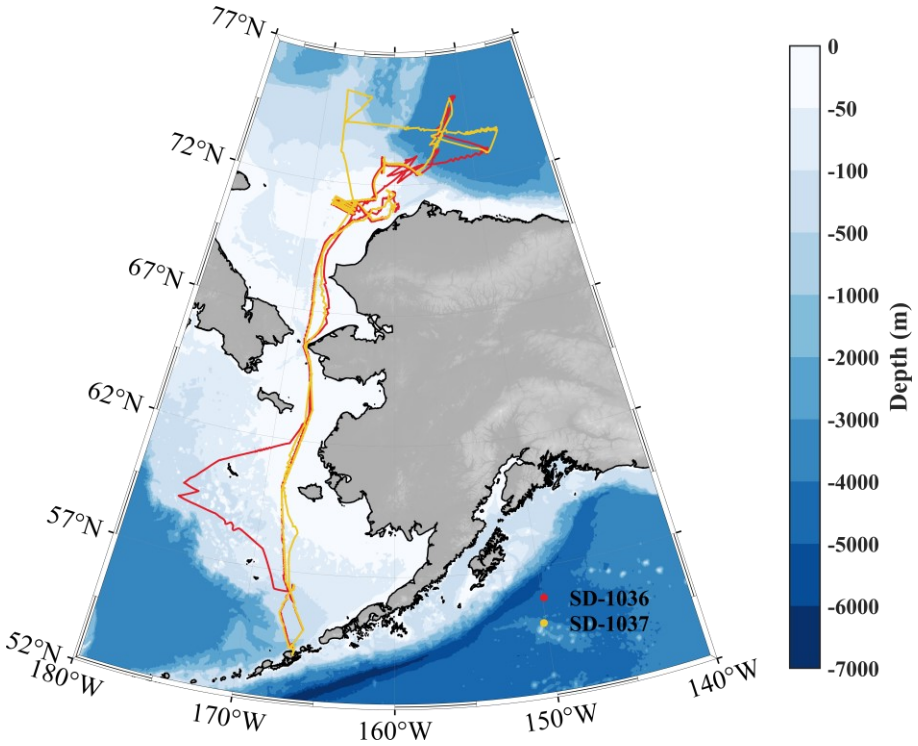

Fig. 2. The tracks of the two NASA-funded Saildrone vehicles, SD-1036 (red line) and SD-1037 (yellow line), during the 2019 Arctic Cruise from 15 May to 11 October. The background is the ocean bathymetry using the ETOPO1 dataset, a 1-arc minute global relief model of Earth's surface, available at: https://www.ngdc.noaa.gov/mgg/global/global.html.

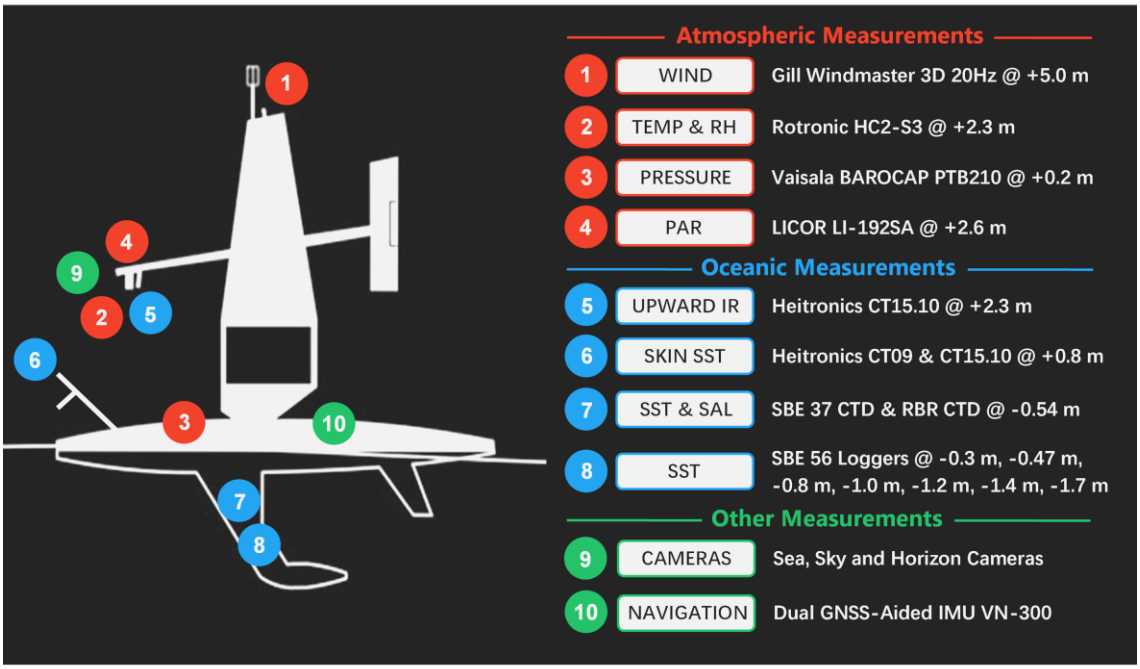

Fig. 3. Schematic diagram of the meteorological and oceanographic sensors mounted on Saildrones SD-1036 and SD-1037. Here, only the sensors introduced in this paper are listed.

Table 1. Comparison of SST_{depth} from different instruments mounted on Saildrones at -0.54 m depth. Measurements taken when the vehicle was close to sea ice are removed. The Sea-Bird CTD, RBR CTD, RBR T.ODO are denoted as SBE, RBR and O_2 respectively. The statistics of temperature difference (K) are given as the mean, median, standard deviation (STD) and robust standard deviation (RSD).

Type of sensor differences	Vehicle	Statistics				
		Mean	Median	STD	RSD	Number
RBR − SBE	1036	-0.0001	0.0026	0.0347	0.0047	171946
	1037	-0.0025	0.0012	0.0551	0.0047	177553
O_2 − SBE	1036	0.0061	0.0050	0.0350	0.0050	171946
	1037	0.0075	0.0075	0.0513	0.0060	177553
O_2 − RBR	1036	0.0060	0.0030	0.0181	0.0052	179685
	1037	0.0102	0.0070	0.0167	0.0059	189373

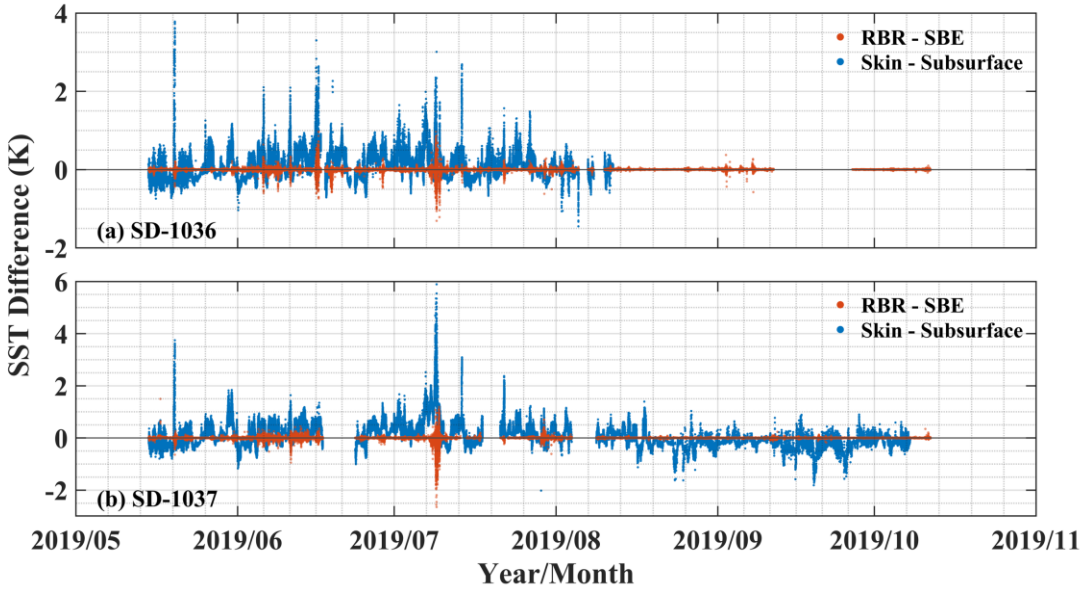

Fig. 4. Time Series of the RBR-SBE (red dots) and skin-subsurface (blue dots) SST differences for (a) SD-1036 and (b) SD-1037. Here the subsurface SSTs represent the measurements from the SBE 56 temperature logger at -0.33 m depth. Note that the SD-1036 SST_{skin} data are missing after 10 August due to the lack of solar radiation causing a reduced power budget leading to the sensors being turned off.

Table 2. Comparisons between the deepest SST measurements and skin and other subsurface SSTs from SD-1036. Signals from periods of thermal stratification and data contaminated by sea ice are excluded. The statistics of temperature differences (K) are given as the mean, median, standard deviation (STD), robust standard deviation (RSD) and mean absolute error (MAE). Note that the SBE 56 logger at -1.04 m was not available during the mission.

Depth and type of sensor differences	Mean	Median	STD	RSD	MAE	Correlation	Number
$\mathbf{SBE_{-0.33} - SBE_{-1.71}}$	0.020	-0.001	0.159	0.008	0.042	0.997	46465
$\mathbf{SBE_{-0.47} - SBE_{-1.71}}$	0.019	-0.001	0.150	0.006	0.039	0.998	46465
$\mathbf{SBE_{-0.81} - SBE_{-1.71}}$	0.016	-0.000	0.124	0.006	0.033	0.998	46465
$\mathbf{SBE_{-1.20} - SBE_{-1.71}}$	0.010	-0.000	0.079	0.005	0.023	0.999	46465
$\mathbf{SBE_{-1.42} - SBE_{-1.71}}$	0.006	-0.000	0.051	0.004	0.016	1.000	46465
$\mathbf{SBE_{-0.54} - SBE_{-1.71}}$	0.018	-0.000	0.143	0.006	0.039	0.998	46013
$\mathbf{RBR_{-0.54} - SBE_{-1.71}}$	0.019	0.002	0.142	0.005	0.037	0.998	46465
$\mathbf{O_{2\,-0.54} - SBE_{-1.71}}$	0.028	0.006	0.143	0.009	0.043	0.998	46465
$\mathbf{CT15_{skin} - SBE_{-1.71}}$	-0.149	-0.156	0.220	0.161	0.199	0.995	46465

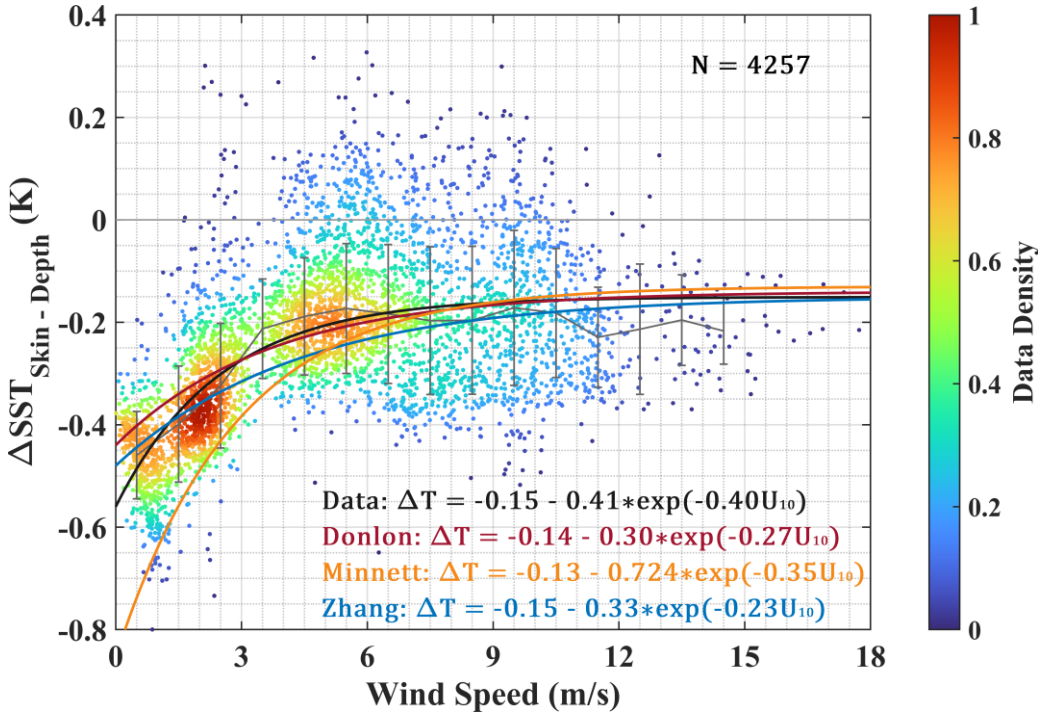

Fig. 5. Nighttime SD-1036 and SD-1037 SST_{skin} minus $SST_{-1.71\ m}$ as a function of 10 m wind speed. The least squares fitted curve is shown in black, and the formulas from *Donlon et al.* (2002), *Minnett et al.* (2011) and *Zhang, H et al.* (2020) are plotted in red, saffron and blue. The mean and standard deviation of temperature differences, calculated at 1 m/s intervals, are shown as gray lines and error bars respectively.

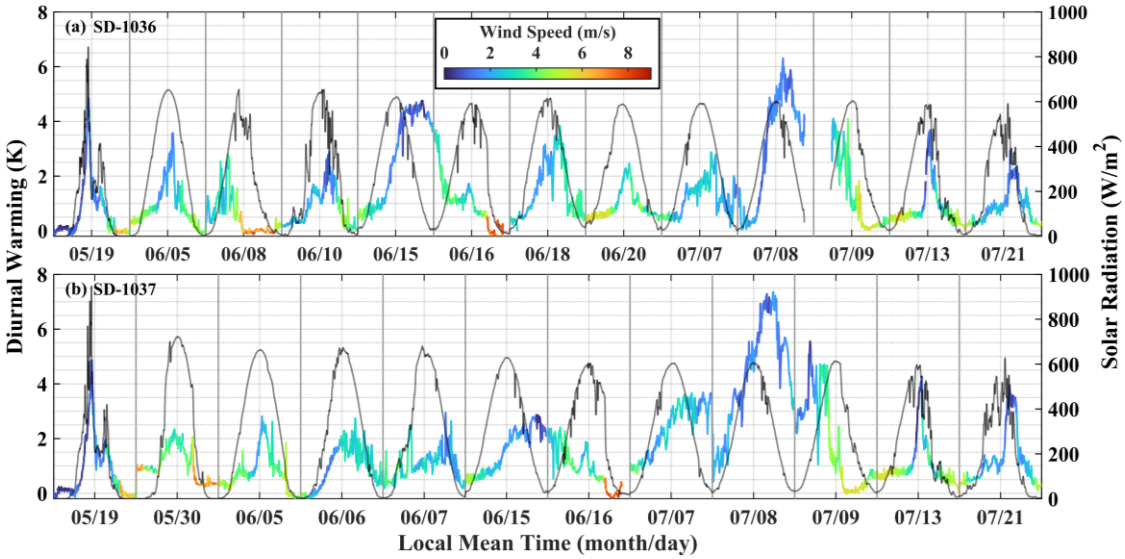

Fig. 6. Diurnal warming (colored line; left axis scale) and solar radiation (black line; right axis scale) as a function of local mean time (LMT) for days with significant warming amplitudes (> 2 K) observed by (a) SD-1036 and (b) SD-1037. The data are shown at 5-min intervals. The vertical grey lines separate each day. The diurnal warming signals are colored by simultaneously measured wind speeds.

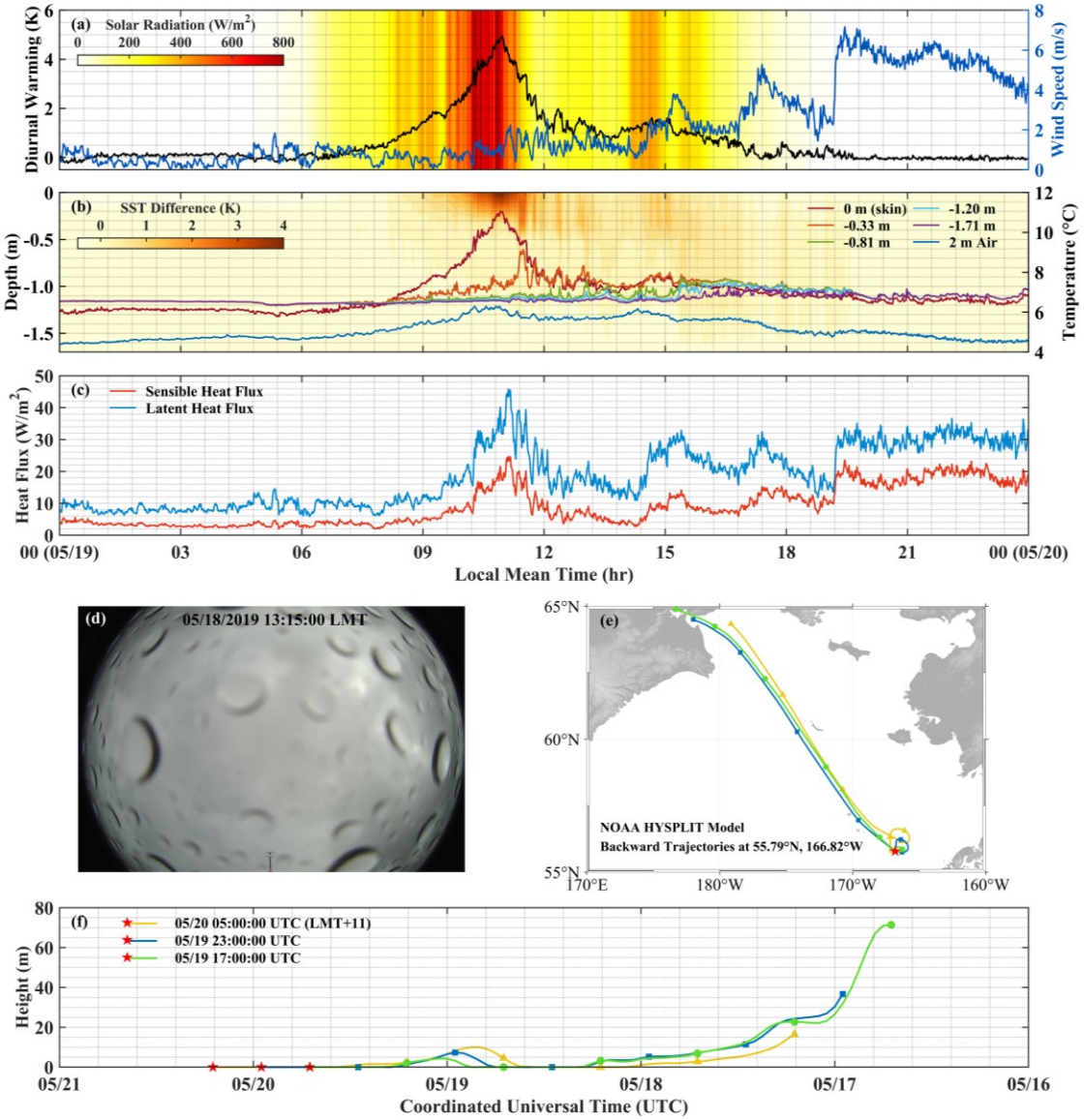

Fig. 7. The diurnal warming event observed by SD-1036 on 19 May 2019 with local time shown in hours. (a) Surface diurnal warming amplitude (black line) is shown with the scale on the left axis and the wind speed (blue line) is shown with the scale on the right axis. The background is colored by the incoming solar radiation. (b) Vertical upper-ocean temperature profile using the deepest $SST_{-1.71\ m}$ as a baseline is plotted as the background with the depth scale shown on the left axis. SST_{skin} and subsurface SSTs (colored lines) measured at different depths are given by the scales on the right axis. (c) Sensible (red line) and latent (blue line) heat fluxes are calculated by the COARE bulk flux algorithm version 3.6 (*Edson et al.*, 2013; *Fairall et al.*, 2003). The heat flux is defined as positive upward. (d) The image taken by the up-looking camera onboard at 13:15 LMT on 18 May 2019, indicating there was rainfall before the occurrence of diurnal warming. (e) Backward atmospheric trajectories at three moments during the warming event are modeled by NOAA HYSPLIT. The red star represents the source of the start location. (f) The height of air along each trajectory output from HYSPLIT is shown in colors consistent with (e). Camera image courtesy Saildrone. Used with express permission.

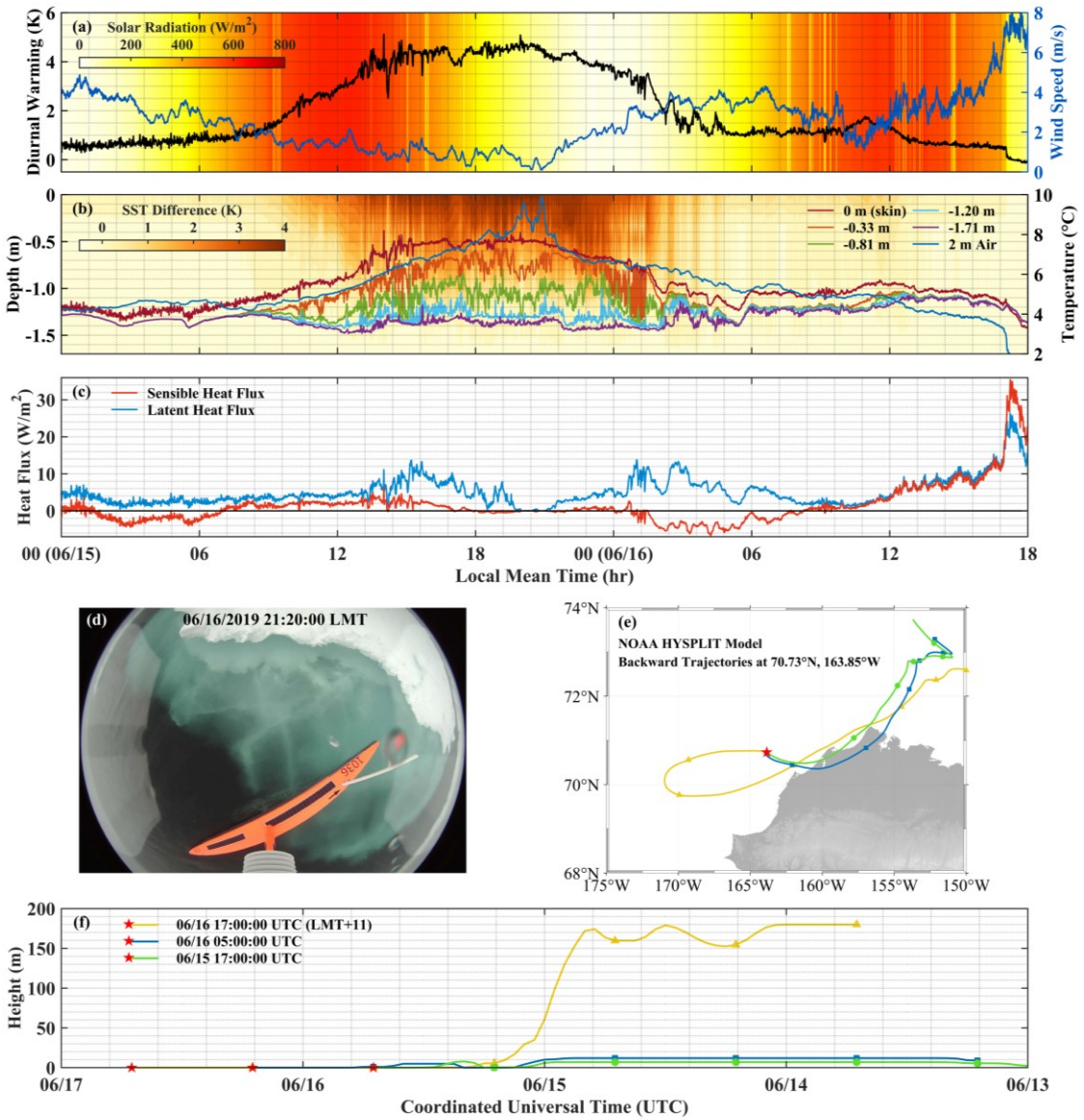

Fig. 8. As Figure 7, but for the diurnal warming event on 15-16 June 2019 observed by SD-1036. Camera image courtesy Saildrone. Used with express permission.

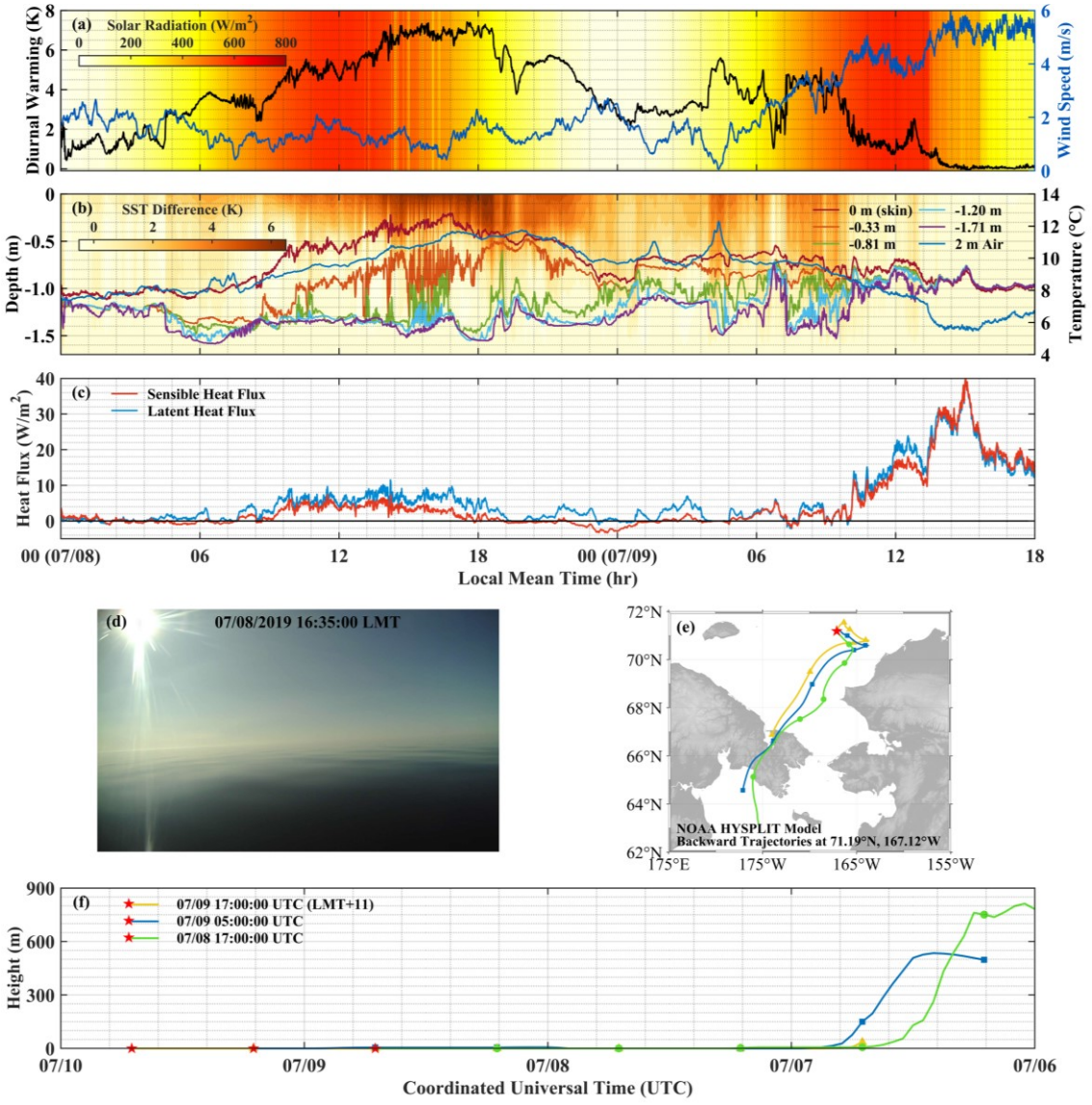

Fig. 9. As Figure 7, but for the diurnal warming event on 8-9 July 2019 observed by SD-1037. Camera image courtesy Saildrone. Used with express permission.

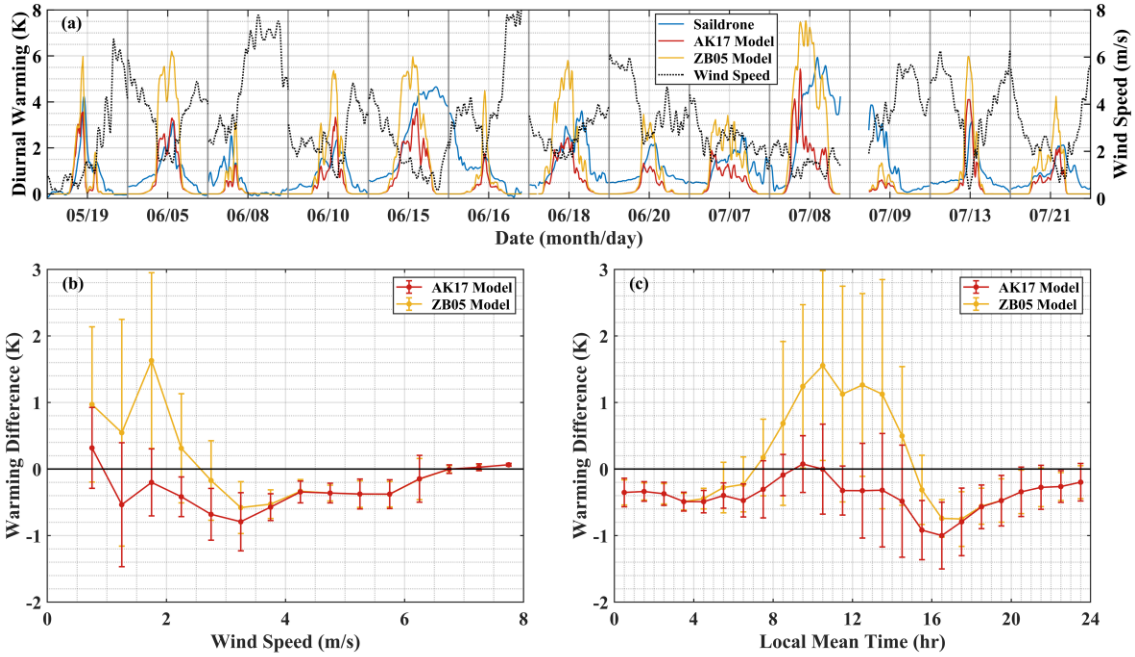

Fig. 10. (a) Diurnal warming events observed by SD-1036 (blue line), simulated by AK17 (red line) and ZB05 (yellow line) with scale are shown on the left axis. The 10 m wind speeds (black dotted line) converted from Saildrone measurements with scale are shown on the right axis. Model-Saildrone diurnal warming differences (removing the consecutive days) are plotted as a function of (b) 10 m wind speed and (c) local time in hour. The dots and error bars indicate the mean and robust standard deviation of the differences, calculated at 0.5 m/s and 1 hr intervals.

Table 3. Distribution of the daily maximum diurnal warming for the effective days measured by SD-1036 and SD-1037.

	<1 K	1~2 K	2~3 K	3~4 K	4~5 K	>5 K	Total
SD-1036	42	17	12	3	3	2	79
SD-1037	64	32	8	4	2	2	112

References

Akella, S., Todling, R., and Suarez, M. (2017), Assimilation for skin SST in the NASA GEOS atmospheric data assimilation system, *Quarterly Journal of the Royal Meteorological Society*, *143*(703), 1032-1046, doi:https://doi.org/10.1002/qj.2988.

Alappattu, D. P., Wang, Q., Yamaguchi, R., Lind, R. J., Reynolds, M., and Christman, A. J. (2017), Warm layer and cool skin corrections for bulk water temperature measurements for air-sea interaction studies, *Journal of Geophysical Research: Oceans*, *122*(8), 6470-6481, doi:https://doi.org/10.1002/2017JC012688.

Bellenger, H., and Duvel, J.-P. (2009), An Analysis of Tropical Ocean Diurnal Warm Layers, *Journal of Climate*, *22*(13), 3629-3646, doi:10.1175/2008JCLI2598.1.

Böhm, E., Marullo, S., and Santoleri, R. (1991), AVHRR visible-IR detection of diurnal warming events in the western Mediterranean Sea, *International Journal of Remote Sensing*, *12*(4), 695-701, doi:10.1080/01431169108929686.

Brunke, M. A., Zeng, X., Misra, V., and Beljaars, A. (2008), Integration of a prognostic sea surface skin temperature scheme into weather and climate models, *Journal of Geophysical Research: Atmospheres*, *113*(D21), doi:https://doi.org/10.1029/2008JD010607.

Deschamps, P. Y., and Frouin, R. (1984), Large Diurnal Heating of the Sea Surface Observed by the HCMR Experiment, *Journal of Physical Oceanography*, *14*(1), 177-184, doi:10.1175/1520-0485(1984)014<0177:LDHOTS>2.0.CO;2.

Donlon, C. J., Minnett, P. J., Gentemann, C., Nightingale, T. J., Barton, I. J., Ward, B., and Murray, M. J. (2002), Toward improved validation of satellite sea surface skin temperature measurements for climate research, *Journal of Climate*, *15*(4), 353-369, doi:10.1175/1520-0442(2002)015<0353:TIVOSS>2.0.CO;2.

Donlon, C. J., et al. (2007), The global ocean data assimilation experiment high-resolution sea surface temperature pilot project, *Bulletin of the American Meteorological Society*, *88*(8), 1197-1214, doi:10.1175/BAMS-88-8-1197.

Eastwood, S., Le Borgne, P., Péré, S., and Poulter, D. (2011), Diurnal variability in sea surface temperature in the Arctic, *Remote Sensing of Environment*, *115*(10), 2594-2602, doi:https://doi.org/10.1016/j.rse.2011.05.015.

Edson, J. B., Jampana, V., Weller, R. A., Bigorre, S. P., Plueddemann, A. J., Fairall, C. W., Miller, S. D., Mahrt, L., Vickers, D., and Hersbach, H. (2013), On the Exchange of Momentum over the Open Ocean, *Journal of Physical Oceanography*, *43*(8), 1589-1610, doi:10.1175/JPO-D-12-0173.1.

Fairall, C. W., Bradley, E. F., Hare, J. E., Grachev, A. A., and Edson, J. B. (2003), Bulk Parameterization of Air–Sea Fluxes: Updates and Verification for the COARE Algorithm, *Journal of Climate*, *16*(4), 571-591, doi:10.1175/1520-0442(2003)016<0571:BPOASF>2.0.CO;2.

Flament, P., Firing, J., Sawyer, M., and Trefois, C. (1994), Amplitude and Horizontal Structure of a Large Diurnal Sea Surface Warming Event during the Coastal Ocean Dynamics Experiment, *Journal of Physical Oceanography*, *24*(1), 124-139, doi:10.1175/1520-0485(1994)024<0124:AAHSOA>2.0.CO;2.

603 Gentemann, C. L., and Akella, S. (2018), Evaluation of NASA GEOS-ADAS modeled diurnal warming through
604 comparisons to SEVIRI and AMSR2 SST observations, *J Geophys Res Oceans*, *123*(2), 1364-1375,
605 doi:10.1002/2017jc013186.
606 Gentemann, C. L., and Minnett, P. J. (2008), Radiometric measurements of ocean surface thermal variability,
607 *Journal of Geophysical Research: Oceans*, *113*(C8), doi:https://doi.org/10.1029/2007JC004540.
608 Gentemann, C. L., Minnett, P. J., Le Borgne, P., and Merchant, C. J. (2008), Multi-satellite measurements of
609 large diurnal warming events, *Geophysical Research Letters*, *35*(22), doi:10.1029/2008GL035730.
610 Gentemann, C. L., et al. (2018), Arctic MISST: Multi-sensor Improved Sea Surface Temperature: Continuing
611 the GHRSST Partnership and Improving Arctic data, in *AGU Fall Meeting*, edited, pp. A24K-11,
612 Washington, D.C., doi:https://ui.adsabs.harvard.edu/abs/2018AGUFM.A24K..11G.
613 Gentemann, C. L., Minnett, P. J., and Ward, B. (2009), Profiles of ocean surface heating (POSH): A new model
614 of upper ocean diurnal warming, *Journal of Geophysical Research: Oceans*, *114*(C7),
615 doi:https://doi.org/10.1029/2008JC004825.
616 Gentemann, C. L., et al. (2020), Saildrone: Adaptively Sampling the Marine Environment, *Bulletin of the*
617 *American Meteorological Society*, *101*(6), E744-E762, doi:10.1175/bams-d-19-0015.1.
618 Halpern, D., and Reed, R. K. (1976), Heat Budget of the Upper Ocean Under Light Winds, *Journal of Physical*
619 *Oceanography*, *6*(6), 972-975, doi:10.1175/1520-0485(1976)006<0972:HBOTUO>2.0.CO;2.
620 Hodges, B. A., and Fratantoni, D. M. (2014), AUV Observations of the Diurnal Surface Layer in the North
621 Atlantic Salinity Maximum, *Journal of Physical Oceanography*, *44*(6), 1595-1604, doi:10.1175/JPO-
622 D-13-0140.1.
623 Høyer, J. L., Karagali, I., Dybkjær, G., and Tonboe, R. (2012), Multi sensor validation and error characteristics
624 of Arctic satellite sea surface temperature observations, *Remote Sensing of Environment*, *121*, 335-346,
625 doi:https://doi.org/10.1016/j.rse.2012.01.013.
626 Jia, C., and Minnett, P. J. (2020), High latitude sea surface temperatures derived from MODIS infrared
627 measurements, *Remote Sensing of Environment*, *251*, 112094,
628 doi:https://doi.org/10.1016/j.rse.2020.112094.
629 Jia, C., Minnett, P. J., Szczodrak, M., and Izaguirre, M. (2022), High Latitude Sea Surface Skin Temperatures
630 Derived From Saildrone Infrared Measurements, *IEEE Transactions on Geoscience and Remote Sensing*,
631 *Under Review*.
632 Karagali, I., Høyer, J., and Hasager, C. (2012), SST diurnal variability in the North Sea and the Baltic Sea,
633 *Remote Sensing of Environment*, *121*, 159-170, doi:https://doi.org/10.1016/j.rse.2012.01.016.
634 Kawai, Y., and Wada, A. (2007), Diurnal sea surface temperature variation and its impact on the atmosphere and
635 ocean: A review, *Journal of Oceanography*, *63*(5), 721-744, doi:10.1007/s10872-007-0063-0.
636 Kennedy, J. J., Brohan, P., and Tett, S. F. B. (2007), A global climatology of the diurnal variations in sea-surface
637 temperature and implications for MSU temperature trends, *Geophysical Research Letters*, *34*(5),
638 doi:https://doi.org/10.1029/2006GL028920.
639 Key, E. L., Minnett, P. J., and Jones, R. A. (2004), Cloud distributions over the coastal Arctic Ocean: surface-
640 based and satellite observations, *Atmospheric Research*, *72*(1), 57-88,
641 doi:https://doi.org/10.1016/j.atmosres.2004.03.029.

Luo, B., Minnett, P. J., Szczodrak, M., and Akella, S. (2022), Regional and Seasonal Variability of the Oceanic Thermal Skin Effect, *Journal of Geophysical Research: Oceans*, *127*(5), e2022JC018465, doi:https://doi.org/10.1029/2022JC018465.

Matthews, A. J., Baranowski, D. B., Heywood, K. J., Flatau, P. J., and Schmidtko, S. (2014), The Surface Diurnal Warm Layer in the Indian Ocean during CINDY/DYNAMO, *Journal of Climate*, *27*(24), 9101-9122, doi:10.1175/JCLI-D-14-00222.1.

McWilliams, J. C., and Sullivan, P. P. (2000), Vertical Mixing by Langmuir Circulations, *Spill Science & Technology Bulletin*, *6*(3), 225-237, doi:https://doi.org/10.1016/S1353-2561(01)00041-X.

Meinig, C., et al. (2019), Public–Private Partnerships to Advance Regional Ocean-Observing Capabilities: A Saildrone and NOAA-PMEL Case Study and Future Considerations to Expand to Global Scale Observing, *Frontiers in Marine Science*, *6*(448), doi:10.3389/fmars.2019.00448.

Meinig, C., Lawrence-Slavas, N., Jenkins, R., and Tabisola, H. M. (2015), The use of Saildrones to examine spring conditions in the Bering Sea: Vehicle specification and mission performance, paper presented at OCEANS 2015-MTS, IEEE, Washington DC, USA.

Merchant, C. J., Filipiak, M. J., Le Borgne, P., Roquet, H., Autret, E., Piollé, J. F., and Lavender, S. (2008), Diurnal warm-layer events in the western Mediterranean and European shelf seas, *Geophysical Research Letters*, *35*(4), doi:https://doi.org/10.1029/2007GL033071.

Minnett, P. J. (2003), Radiometric measurements of the sea-surface skin temperature: the competing roles of the diurnal thermocline and the cool skin, *International Journal of Remote Sensing*, *24*(24), 5033-5047, doi:10.1080/0143116031000095880.

Minnett, P. J., and Kaiser-Weiss, A. (2012), Near-surface oceanic temperature gradients, *GHRSST Discussion Doc*, *7*, doi:https://www.ghrsst.org/wp-content/uploads/2016/10/SSTDefinitionsDiscussion.pdf.

Minnett, P. J., Smith, M., and Ward, B. (2011), Measurements of the oceanic thermal skin effect, *Deep Sea Research Part II: Topical Studies in Oceanography*, *58*(6), 861-868, doi:https://doi.org/10.1016/j.dsr2.2010.10.024.

Mordy, C. W., et al. (2017), Advances in Ecosystem Research: Saildrone Surveys of Oceanography, Fish, and Marine Mammals in the Bering Sea, *Oceanography*, *30*(2), 113-115, doi:http://www.jstor.org/stable/26201857.

Nunez, M., Cantin, N., Steinberg, C., van Dongen-Vogels, V., and Bainbridge, S. (2022), Correcting PAR Data from Photovoltaic Quantum Sensors on Remote Weather Stations on the Great Barrier Reef, *Journal of Atmospheric and Oceanic Technology*, *39*(4), 425-448, doi:10.1175/JTECH-D-21-0095.1.

Peralta-Ferriz, C., and Woodgate, R. A. (2015), Seasonal and interannual variability of pan-Arctic surface mixed layer properties from 1979 to 2012 from hydrographic data, and the dominance of stratification for multiyear mixed layer depth shoaling, *Progress in Oceanography*, *134*, 19-53, doi:https://doi.org/10.1016/j.pocean.2014.12.005.

Pithan, F., and Mauritsen, T. (2014), Arctic amplification dominated by temperature feedbacks in contemporary climate models, *Nature Geoscience*, *7*(3), 181-184, doi:10.1038/ngeo2071.

Price, J. F., Weller, R. A., and Pinkel, R. (1986), Diurnal cycling: Observations and models of the upper ocean response to diurnal heating, cooling, and wind mixing, *Journal of Geophysical Research: Oceans*, *91*(C7), 8411-8427, doi:https://doi.org/10.1029/JC091iC07p08411.

682 Saunders, P. M. (1967), The Temperature at the Ocean-Air Interface, *Journal of Atmospheric Sciences*, *24*(3),
683 269-273, doi:10.1175/1520-0469(1967)024<0269:TTATOA>2.0.CO;2.
684 Schluessel, P., Emery, W. J., Grassl, H., and Mammen, T. (1990), On the bulk-skin temperature difference and
685 its impact on satellite remote sensing of sea surface temperature, *Journal of Geophysical Research:*
686 *Oceans*, *95*(C8), 13341-13356, doi:https://doi.org/10.1029/JC095iC08p13341.
687 Shukla, J. (1998), Predictability in the Midst of Chaos: A Scientific Basis for Climate Forecasting, *Science*,
688 *282*(5389), 728-731, doi:10.1126/science.282.5389.728.
689 Shupe, M. D., Walden, V. P., Eloranta, E., Uttal, T., Campbell, J. R., Starkweather, S. M., and Shiobara, M.
690 (2011), Clouds at Arctic Atmospheric Observatories. Part I: Occurrence and Macrophysical Properties,
691 *Journal of Applied Meteorology and Climatology*, *50*(3), 626-644, doi:10.1175/2010JAMC2467.1.
692 Stein, A. F., Draxler, R. R., Rolph, G. D., Stunder, B. J. B., Cohen, M. D., and Ngan, F. (2015), NOAA's
693 HYSPLIT Atmospheric Transport and Dispersion Modeling System, *Bulletin of the American*
694 *Meteorological Society*, *96*(12), 2059-2077, doi:10.1175/BAMS-D-14-00110.1.
695 Stommel, H., and Woodcock, A. H. (1951), Diurnal heating of the surface of the Gulf of Mexico in the spring of
696 1942, *Eos, Transactions American Geophysical Union*, *32*(4), 565-571,
697 doi:https://doi.org/10.1029/TR032i004p00565.
698 Stramma, L., Cornillon, P., Weller, R. A., Price, J. F., and Briscoe, M. G. (1986), Large Diurnal Sea Surface
699 Temperature Variability: Satellite and In Situ Measurements, *Journal of Physical Oceanography*, *16*(5),
700 827-837, doi:10.1175/1520-0485(1986)016<0827:LDSSTV>2.0.CO;2.
701 Sverdrup, H. U., Johnson, M. W., and Fleming, R. H. (1942), *The Oceans: Their physics, chemistry, and general*
702 *biology*, Prentice-Hall, Inc., New York.
703 Takaya, Y., Bidlot, J.-R., Beljaars, A. C. M., and Janssen, P. A. E. M. (2010), Refinements to a prognostic scheme
704 of skin sea surface temperature, *Journal of Geophysical Research: Oceans*, *115*(C6),
705 doi:https://doi.org/10.1029/2009JC005985.
706 Vazquez-Cuervo, J., Gomez-Valdes, J., Bouali, M., Miranda, L. E., Van der Stocken, T., Tang, W., and
707 Gentemann, C. (2019), Using Saildrones to Validate Satellite-Derived Sea Surface Salinity and Sea
708 Surface Temperature along the California/Baja Coast, *Remote Sensing*, *11*(17), doi:10.3390/rs11171964.
709 Vincent, R. F., Marsden, R. F., Minnett, P. J., and Buckley, J. R. (2008b), Arctic waters and marginal ice zones:
710 2. An investigation of arctic atmospheric infrared absorption for advanced very high resolution
711 radiometer sea surface temperature estimates, *Journal of Geophysical Research: Oceans*, *113*(C8),
712 doi:10.1029/2007JC004354.
713 Vincent, R. F., Marsden, R. F., Minnett, P. J., Creber, K. A. M., and Buckley, J. R. (2008a), Arctic waters and
714 marginal ice zones: A composite Arctic sea surface temperature algorithm using satellite thermal data,
715 *Journal of Geophysical Research: Oceans*, *113*(C4), doi:10.1029/2007JC004353.
716 Ward, B., Fristedt, T., Callaghan, A. H., Sutherland, G., Sanchez, X., Vialard, J., and Doeschate, A. t. (2014),
717 The Air–Sea Interaction Profiler (ASIP): An Autonomous Upwardly Rising Profiler for Microstructure
718 Measurements in the Upper Ocean, *Journal of Atmospheric and Oceanic Technology*, *31*(10), 2246-
719 2267, doi:10.1175/JTECH-D-14-00010.1.
720 Xu, F., and Ignatov, A. (2014), In situ SST Quality Monitor (iQuam), *Journal of Atmospheric and Oceanic*
721 *Technology*, *31*(1), 164-180, doi:10.1175/JTECH-D-13-00121.1.

Zeng, X., and Beljaars, A. (2005), A prognostic scheme of sea surface skin temperature for modeling and data assimilation, *Geophysical Research Letters*, *32*(14), doi:https://doi.org/10.1029/2005GL023030.

Zhang, D., Cronin, M. F., Meinig, C., Farrar, J. T., Jenkins, R., Peacock, D., Keene, J., Sutton, A., and Yang, Q. (2019), Comparing air-sea flux measurements from a new unmanned surface vehicle and proven platforms during the SPURS-2 field campaign, *Oceanography*, *32*(2), 122-133.

Zhang, H., Beggs, H., Ignatov, A., and Babanin, A. V. (2020), Nighttime Cool Skin Effect Observed from Infrared SST Autonomous Radiometer (ISAR) and Depth Temperatures, *Journal of Atmospheric and Oceanic Technology*, *37*(1), 33-46, doi:10.1175/jtech-d-19-0161.1.